Evaluation of 1-D and 3-D seismic models of the Pacific lower mantle with S, SKS, and SKKS traveltimes and amplitudes

Michael S. Thorne,[1] Yang Zhang,[2] and Jeroen Ritsema[2]

Received 5 September 2012; revised 11 December 2012; accepted 11 December 2012; published 1 March 2013.

[1] In this study, we analyzed the seismic phases S, SKS, and SKKS from 31 deep-focus earthquakes in the Tonga-Fiji region recorded in North America between epicentral distances of 85° and 120°. The differential traveltimes and amplitude ratios for these phases reveal clear epicentral distance trends not predicted by standard one-dimensional (1-D) reference Earth models. The increase of the S/SKS amplitude ratio up to a factor of 10 is accompanied by an increase of the S-SKS differential traveltime of up to 10 s. SKKS-SKS differential traveltimes of 2–3 s and SKKS/SKS amplitude ratios of a factor of 2–4 across the epicentral range have maxima near 107°. We examined these observations using full (1-D and 3-D) waveforms for three 1-D seismic velocity profiles for the central Pacific region and for the tomographic model S40RTS including modifications: different regularization parameters, great-circle path azimuthal variation, strength of *S* wave velocity perturbations, *S* wave velocity gradients in the lower mantle, and ultra–low velocity zones. To explain these data, we constructed a hybrid model that combines both features of S40RTS and short-wavelength features from the 1-D profiles. The large-scale seismic structure is represented by S40RTS. Embedded within S40RTS are a 20 km thick ultra–low velocity zone at the core-mantle boundary near the source side and a 200 km thick negative velocity gradient zone near the receiver side of the paths. Our analysis demonstrates that the *S* wave velocity structure of the Pacific large low shear-velocity province cannot be interpreted solely by global tomographic or regional modeling approaches in exclusion of each other.

Citation: Thorne, M. S., Y. Zhang, and J. Ritsema (2013), Evaluation of 1-D and 3-D seismic models of the Pacific lower mantle with S, SKS, and SKKS traveltimes and amplitudes, *J. Geophys. Res. Solid Earth*, *118*, 985–995, doi:10.1002/jgrb.50054.

1. Introduction

[2] Seismic modeling of the lower mantle can be characterized by two approaches. The first approach involves imaging the large-scale (>1000 km) three-dimensional (3-D) structure of the Earth's interior by tomographic and forward modeling of high-amplitude phase traveltimes and normal-mode frequencies. These 3-D images provide a global perspective revealing two broad, low seismic velocity anomalies in the lower mantle [e.g., *Garnero and McNamara*, 2008; *Dziewonski et al*., 2010]. These regions have been termed large low shear-velocity provinces (LLSVPs) and exist above the core-mantle boundary (CMB) beneath the central Pacific Ocean and Africa [e.g., *He and Wen*, 2009]. Recent studies show they have relatively sharp margins extending from the CMB to at least 1000 km into the mantle [e.g., *To et al*., 2005; *Takeuchi et al*., 2008; *Sun et al*., 2010]. These LLSVPs may be piles of compositionally distinct material [e.g., *Ni and Helmberger*, 2003; *Trampert et al*., 2004; *Bull et al*., 2009] or signatures of thermal upwelling [e.g., *Schuberth et al*., 2009; *Simmons et al*., 2009; *Davies et al*., 2012].

[3] The second seismic approach involves waveform modeling and array processing of low-amplitude signals. This approach typically renders one-dimensional (1-D) profiles of seismic velocity for well-sampled mantle regions. The profiles reveal mantle layering [e.g., *Russell et al*., 2001] due to the mineral phase changes [e.g., *Hernlund et al*., 2005; *Lay et al*., 2006], the presence of melt layers [e.g., *Williams and Garnero*, 1996; *Hernlund and Tackley*, 2007; *Hutko et al*., 2009], and the shear-wave anisotropy [e.g., *Pulliam and Sen*, 1998; *Ford et al*., 2006]. See *Rost and Thomas* [2009] and *Lay and Garnero* [2011] for reviews.

[4] Frequently, seismologists assume that the tomographic images and the wave speed profiles provide complementary views in which "fine-scale" (<500 km) layering of D″ is embedded within the large-scale (>1000 km) convecting lower mantle. As an example, Figure 1 shows 1-D and 3-D images of the lower mantle beneath the Pacific Ocean. In Figure 1a, an SW–NE-oriented cross section through tomography model S40RTS [*Ritsema et al*., 2011] shows the Pacific LLSVP extending from the CMB halfway into the mid-mantle between Tonga-Fiji and North America. Figure 1b shows the Preliminary Reference Earth Model (PREM) [*Dziewonski and Anderson*, 1981] and three other 1-D *S* wave velocity profiles for the lower mantle beneath the central Pacific Ocean.

[1]Department of Geology and Geophysics, University of Utah, Salt Lake City, Utah, USA.
[2]Department of Earth and Environmental Sciences, University of Michigan, Ann Arbor, Michigan, USA.

Corresponding author: M. S. Thorne, Department of Geology and Geophysics, University of Utah, Salt Lake City, Utah, USA. (michael.thorne@utah.edu)

2169-9313/13/10.1002/jgrb.50054

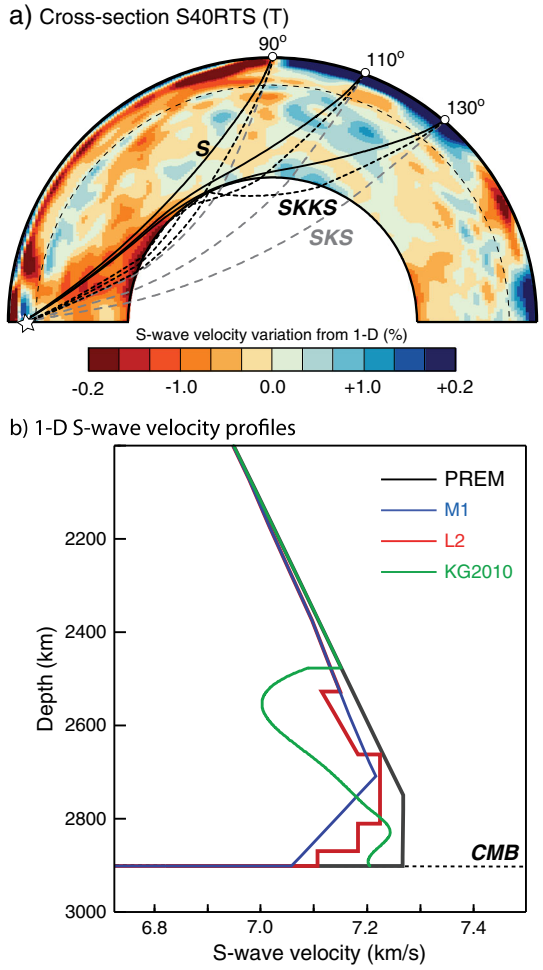

Figure 1. (a) Shear velocity perturbation from PREM in a vertical cross section (*T*) through the mantle according to model S40RTS [*Ritsema et al.*, 2011]. The cross section *T* includes the Fiji-Tonga source region (indicated by the star) and North America. The solid, dashed, and dotted lines are S, SKS, and SKKS raypaths for epicentral distances of 90°, 110°, and 130° calculated using the M1 [*Ritsema et al.*, 1997] velocity profile. (b) Shear-velocity profiles for (black) PREM [*Dziewonski and Anderson*, 1981], (blue) M1 [*Ritsema et al.*, 1997], (red) L2 [*Lay et al.*, 2006], and (green) KG10 (*Kawai and Geller*, 2010) for the Central Pacific.

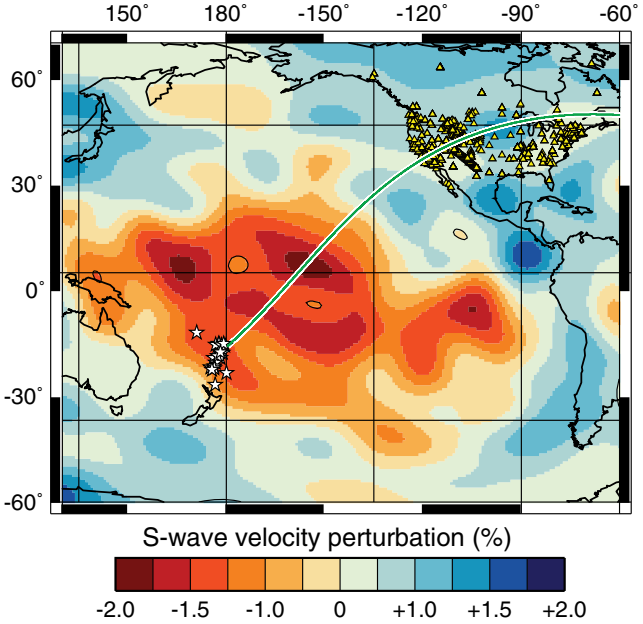

Figure 2. Event-receiver geometry, with the average great circle path indicated by the light blue line. The events (white stars) and receivers (yellow triangles) are from the Fiji-Tonga and North America regions, respectively.

The discontinuities, velocity gradients, and absolute *S* wave velocities in M1 [*Ritsema et al.*, 1997], L2 [*Lay et al.*, 2006], and KG10 [*Kawai and Geller*, 2010] have been attributed to phase transitions in perovskite and anomalous thermal gradients at the base of the Pacific LLSVP [e.g., *Tsuchiya et al.*, 2004; *Hernlund et al.*, 2005; *Tsuchiya and Tsuchiya*, 2006].

[5] In this paper, we illustrate how traveltimes and amplitudes can be influenced by both large- and fine-scale seismic heterogeneity. We focus on the trans-Pacific cross section of the lower mantle shown in Figure 1, which has been studied thoroughly thanks to the large number of high-quality recordings of deep-focus earthquakes in the Fiji-Tonga region at seismic networks across Canada and the United States. The cross section shown in Figure 1 cuts through the center of the Pacific LLSVP as shown in Figure 2. We hypothesize that the LLSVP in Figure 1a and the 1-D velocity profiles of Figure 1b are models of the same low velocity structure and that the profound differences in the dimensions are accentuated by the different modeling procedures.

[6] We test our hypothesis by analyzing waveform predictions for the 1-D profiles, S40RTS, and a series of modifications to S40RTS. We evaluate how the traveltimes and amplitudes of S, SKS, and SKKS depend on (1) the applied regularization to S40RTS, (2) the great circle path azimuthal variation, (3) the radial *S* wave velocity gradients in D″, (4) the magnitude of *S* wave velocity anomalies tomographically recovered, and (5) the influence of ultra–low velocity zone (ULVZ) layering.

2. Traveltimes and Amplitudes

[7] We analyzed traveltimes and amplitudes of the seismic phases S, SKS, and SKKS recorded in North America. The raypaths of S, SKS, and SKKS are shown in Figure 1a for the entire epicentral distance range considered in this study. In the lower mantle, the direct *S* wave passes through the center of the LLSVP and propagates nearly parallel to the CMB in D″ with a path length greater than roughly 1000 km for epicentral distances larger than 110°. SKKS also passes through the LLSVP but intersects D″ at a relatively steep angle. SKS is steeper than SKKS and skirts the southwestern margin of the LLSVP.

[8] We analyzed traveltime differences and amplitude ratios of SKKS and S relative to SKS. Relative traveltime and amplitude ratios are not strongly influenced by upper-mantle heterogeneity, earthquake mislocation, or uncertainties in the seismic moment tensor. Using SKS as a reference phase, we denote the traveltime differences as

$$\delta T_S = T^{\mathrm{obs}}_{S-\mathrm{SKS}} - T^{\mathrm{ref}}_{S-\mathrm{SKS}}, \quad (1)$$

and

$$\delta T_{\mathrm{SKKS}} = T^{\mathrm{obs}}_{\mathrm{SKKS}-\mathrm{SKS}} - T^{\mathrm{ref}}_{\mathrm{SKKS}-\mathrm{SKS}}. \quad (2)$$

[9] The amplitude ratios are defined as

$$\delta A_S = log_{10}\left(\frac{A_S}{A_{\mathrm{SKS}}}\right)^{\mathrm{obs}} - log_{10}\left(\frac{A_S}{A_{\mathrm{SKS}}}\right)^{\mathrm{ref}}, \quad (3)$$

and

$$\delta A_{\mathrm{SKKS}} = log_{10}\left(\frac{A_{\mathrm{SKKS}}}{A_{\mathrm{SKS}}}\right)^{\mathrm{obs}} - log_{10}\left(\frac{A_{\mathrm{SKKS}}}{A_{\mathrm{SKS}}}\right)^{\mathrm{ref}}. \quad (4)$$

[10] The reference (i.e., second) terms in the right-hand side of equations (1), (2), (3), and (4) are computed using PREM [*Dziewonski and Anderson*, 1981] and Global CMT source parameters. Thus, traveltime differences and amplitude ratios are defined as anomalies with respect to PREM. Values of δT and δA equal to 0 mean that the measurements are identical to PREM predicted values.

2.1. Fiji-Tonga Recordings in North America

[11] We analyzed data from 31 events (1995–2007) in the Tonga-Fiji region with moment magnitudes larger than 6 (Table 1) and focal depths greater than 300 km. The event epicenters have latitudes between 13°S and 32°S and longitudes between 170°E and 176°W (Figure 2). We analyzed the broadband seismograms of these events recorded at the Transportable Array, ANSA Backbone, IRIS/GSN, CNSN, TriNET, BDSN, and PASSCAL networks in North America at epicentral distances between 80° and 130° and source azimuths between 30° and 60°. However, most stations in the United States are within the azimuth range of 45°–60°.

[12] Data processing steps include low-pass filtering ($T > 5$ s), instrument deconvolution, and rotation to radial (R) and transverse (T) components. We inspected all traces visually to select waveforms without obvious source complexity.

[13] Recorded and synthetic waveforms for the Tonga-Fiji earthquake of 16 October 2007, $M_W = 6.6$, at stations CMB (84.7°), CCM (104.6°), and HRV (120.2°) are shown in Figure 3. These records show the prominent waveform characteristics of our data set. Namely, S, SKS, and SKKS arrivals are delayed with respect to PREM predictions. In addition, the S wave is recorded with an anomalously large amplitude on the radial component. These waveform

Table 1. Fiji-Tonga Earthquakes

Date	Latitude (°S)	Longitude (°E)	Depth (km)	M_W
3 December 1991	26.31	178.57	581.0	6.3
11 July 1992	22.28	−178.51	381.0	7.2
21 April 1993	17.73	179.81	600.0	6.2
7 August 1993	23.87	179.82	555.0	6.7
9 March 1994	17.77	−178.50	564.0	7.6
27 October 1994	25.79	179.35	549.0	6.6
17 January 1995	20.87	−179.23	637.0	6.3
13 April 1995	13.40	170.40	640.0	6.1
5 August 1996	20.69	−178.31	550.0	7.4
19 October 1996	20.41	−178.51	591.0	6.9
25 May 1997	32.12	179.79	333.0	7.1
4 September 1997	26.57	178.34	624.7	6.8
27 January 1998	22.41	179.04	610.1	6.4
29 March 1998	17.55	−179.09	537.2	7.1
16 May 1998	22.23	−179.52	586.1	6.8
26 June 1999	17.96	−178.19	590.4	6.0
13 January 2000	17.61	−178.74	535.0	6.2
4 May 2000	17.91	−178.52	515.8	6.4
14 June 2000	25.52	178.05	604.6	6.4
15 August 2000	31.51	179.73	357.7	6.6
28 April 2001	18.06	−176.94	351.8	6.8
30 June 2002	22.20	179.25	620.4	6.4
19 August 2002	21.70	−179.51	580.0	7.6
4 January 2003	20.57	−177.66	378.0	6.5
5 October 2007	25.19	179.46	509.4	6.5
16 October 2007	25.77	179.53	509.3	6.6
15 January 2008	21.98	−179.54	597.6	6.5
18 April 2008	17.34	−179.02	553.8	6.3
3 July 2008	23.37	−179.78	581.2	6.2
17 July 2008	17.34	−177.31	391.0	6.4
18 February 2009	27.42	−176.33	25.0	7.0

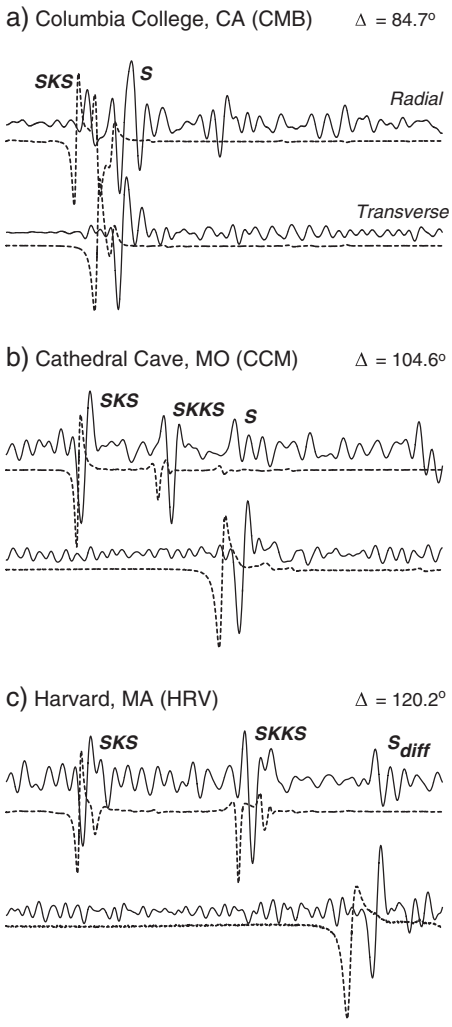

Figure 3. An example of (solid lines) recorded and (dashed lines) synthetic waveforms (velocity) of SKS, SKKS, and S waves at stations (a) CMB, (b) CCM, and (c) HRV for the 16 October 2007 ($H = 512$ km, $M_W = 6.6$) Fiji Islands earthquake. The radial components are plotted above the transverse component waveforms.

attributes are indicative of S, SKS, and SKKS having propagated through a low-velocity structure.

2.2. SKKS-SKS and SKKS/SKS

[14] The measurements of δT_{SKKS} traveltimes and δA_{SKKS} amplitudes are obtained by cross-correlating 30 s long waveforms centered on SKS and SKKS. The SKKS waveform is Hilbert transformed to account for its $\pi/2$ phase shift with respect to SKS. Errors in the measurement have been evaluated following *Tanaka* [2002]. We obtained 477 measurements of δT_{SKKS} and δA_{SKKS} for epicentral distances larger than 90° when SKKS is well developed and separated from SKS.

[15] Figures 4a and 4b show the variation of δT_{SKKS} and δA_{SKKS} as a function of epicentral distance. δA_{SKKS} is positive over the entire distance range increasing to a peak value of approximately 0.5 at an epicentral distance of 107°. The δT_{SKKS} values are also primarily positive, indicating that SKKS is delayed more than SKS. These measurements also peak near an epicentral distance of 107°.

2.3. S-SKS and S/SKS

[16] At diffraction distances (>110° for our study region), S-arrivals on the *T* component (denoted as SH) broaden and S-arrivals on the R component (denoted as SV) have complex wave shapes, thus complicating traveltime and amplitude measurements by waveform correlation. Therefore, we measured δT_S traveltimes (Figure 4c) using SH and SKS onsets and δA_S (Figure 4d) from SV and SKS peak amplitudes [see also *Ritsema et al*., 1997]. Corrections for upper mantle anisotropy have been made using the SKS splitting tables of *Schutt and Humphreys* [2001]. δT_S and δA_S have been measured beginning at 82° and 90°, respectively. We obtained 1174 measurements of δT_S and 823 measurements of δA_S. Both δT_S and δA_S increase monotonously with increasing epicentral distance. δA_S increases from 0 at 85° to ~1.5 at a distance of 120°.

3. Modeling

[17] To understand the observed trends in traveltimes and amplitudes, we analyzed a selection of recently published 1-D profiles and 3-D models derived for the central Pacific region from waveform modeling and tomographic inversion approaches. The models are primarily constrained by broadband recordings in North American from Fiji-Tonga earthquakes and thus sample the same mantle cross section as shown in Figures 2 and 1a.

3.1. One-Dimensional Models

[18] We considered the three 1-D profiles of *S* wave velocity for the central Pacific region, depicted in Figure 1b and discussed in Section 1. Profile M1 [*Ritsema et al*., 1997] was derived from a similar but smaller collection of δT_S and δA_S measurements than used in this study. M1 is identical to PREM to a depth of 2000 km. Below 2000 km, M1 is composed of two linear segments. In the upper segment, the *S* wave velocity decreases linearly to a value 0.5% smaller than PREM at 2700 km depth. Below 2700 km depth, the *S* wave velocity decreases to a value that is 3% lower than PREM at the CMB.

[19] Model KG10 [*Kawai and Geller*, 2010] is based on waveform inversion of S and ScS waveforms. The *S* wave velocity is identical to PREM to a depth of 2500 km. Below 2500 km depth, the *S* wave velocity profile has alternating negative and positive gradients. The *S* wave velocity decreases from 7.08 km/s (the PREM value) at approximately 2471 km depth to 6.99 km/s at approximately 2547 km depth. Between 2547 km and 2819 km, the velocity increases from 6.99 to 7.24 km/s. In the lowermost 70 km of the mantle, the *S* wave velocity decreases to 7.2 km/s at the CMB, a value that is 3.6% lower than the PREM value.

[20] Profile L2 is from *Lay et al*. [2006], who analyzed the *S* wave velocity beneath the central Pacific region from stacks of ScS precursors. In this study, three velocity profiles were determined based on ScS bounce point locations on the CMB. Model L2 is the second of these three velocity profiles

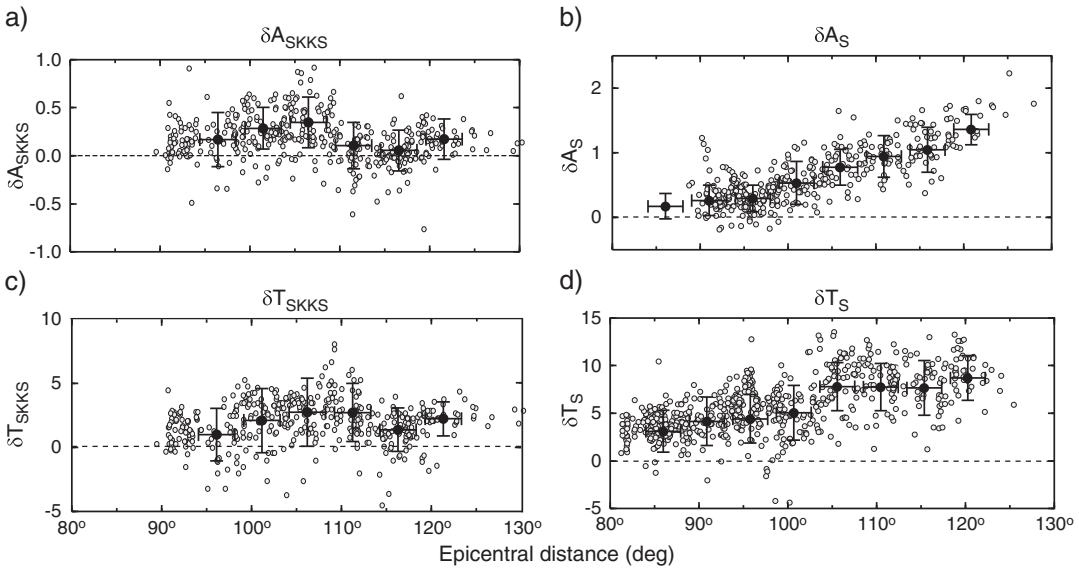

Figure 4. Measurements (gray circles) and average values (including 1σ uncertainties), determined in 5° wide overlapping bins, of (a) δA_{SKKS}, (b) δT_{SKKS}, (c) δT_{SKKS}, and (d) δT_S.

for a 240 km wide sampling region of the lowermost mantle. The *S* wave velocity structure of L2 is similar to M1 but includes several discontinuous *S* wave velocity increases (0.6% at 2655 km depth) and decreases (0.5% at 2520 km, 0.6% at 2800 km, and 1.1% at 2860 km depth).

3.2. Three-Dimensional Models

[21] We analyzed a cross section (which we call *T*) through S40RTS [*Ritsema et al*., 2011], shown in Figure 1a. The midpoint of *T* is at 40°N and 110°W and the great-circle arc crosses the meridian at this midpoint at an angle (i.e., azimuth) of 60° clockwise from North.

[22] We also analyzed several modifications to *T*, summarized in Table 2 and shown in Figure 5. In models T_{H1} and T_{H2}, the *S* wave velocity anomalies are set to be zero within the source side (from 0° to 90°) and receiver side (from 90° to 180°) of the cross section, respectively. T_{H1} and T_{H2} enable us to separate the influence of the LLSVP and the *S* wave velocity structure beneath the northeast Pacific and North America on the observed traveltime and amplitude anomalies.

[23] The cross sections T_{D1} and T_{D2} are based on S40RTS inversions with different applied damping factors. These models let us determine whether the amplitude and traveltime anomalies depend on the strength of *S* wave velocity anomalies in tomographic inversions. T_{D1} is damped more and T_{D2} is damped less than *T*. Therefore, the *S* wave velocity variations in T_{D1} and T_{D2} are about a factor of two weaker and stronger than that in *T*, respectively. In addition, the *S* wave velocity variations are smoothest in T_{D1}. However, T_{D1}, T_{D2}, and *T* yield comparable fit within error to the same data set used in the tomographic inversion. For additional discussion, see *Ritsema et al*. [2007].

[24] Data used in this study are associated with source-receiver paths for a range of azimuths. However, model prediction of traveltimes and amplitudes are based on axisymmetric velocity structures as discussed in the next section. To examine the variability of the amplitude and the traveltime anomalies due to the 3-D nature of *S* wave velocity variations in the lower mantle, we computed waveforms for slightly different cross section through S40RTS. Models T_{A1} and T_{A2} are cross sections drawn with more northerly azimuths of, respectively, 40° and 50°.

Table 2. Models

3-D Models	Remarks
T	S40RTS (see Figure 1b)
T_{H1}	*T* but $\delta V_S = 0$ from 0° to 90°
T_{H2}	*T* but $\delta V_S = 0$ from 90° to 180°
T_{A1}	S40RTS with azimuth 40°
T_{A2}	S40RTS with azimuth 50°
T_{D1}	S40RTS inversion damped weakly
T_{D2}	S40RTS inversion damped strongly
$T_{1.75}$	Negative velocities scaled by 1.75
$T_{2.0}$	Negative velocities scaled by 2.0
$T_{3.0}$	Negative velocities scaled by 3.0
1-D Models	
M1	Ritsema et al. (1997)
L2	Lay et al. (2006)
KG10	Kawai and Geller (2010)
Hybrid Models	
T_{HYB}	*T* plus ULVZ plus M1 (from 40° to 60°)

[25] Previous efforts have suggested that the magnitude of velocity anomalies resolved in tomographic studies is underestimated. For example, *Ni et al*. [2000] scaled tomography model TXBW [*Grand*, 1994], by a factor of 3.0 to model ScS precursors. We also tested the strength of *S* wave velocity anomalies resolved in S40RTS by multiplying the negative velocities in cross section *T* by a constant value. Models $T_{1.75}$, $T_{2.0}$, and $T_{3.0}$ are scaled by 1.75, 2.0, and 3.0 times, respectively.

3.3. PSVaxi and SHaxi Synthetics

[26] The advent of relatively cheap computer clusters has spurred the development of techniques that are capable of solving the seismic wave equation for complex 2-D and 3-D structures on the global scale. For example, the 2-D hybrid approach of computing synthetic seismograms [e.g., *He and Wen*, 2009], the 2-D pseudo-spectral approach [e.g., *Rondenay et al*., 2010; *Cormier*, 2000; *Furumura et al*., 1998] and the 3-D Spectral-Element Method (SEM) approach [*To et al*., 2005; *Ni et al*., 2005] have been used to investigate LLSVP geometry.

[27] Here we used the SHaxi method [*Jahnke et al*., 2008] and its P-SV companion PSVaxi [based on the method of *Igel and Weber*, 1996] to compute the full seismic wavefield of P-SV and SH motions with the correct 3-D geometric spreading. In SHaxi and PSVaxi, the computation is performed on a 2-D grid in the plane of the great-circle arc. The 2-D grid of heterogeneity is expanded to a 3-D spherical geometry by rotating the grid around the radial axis passing through the seismic source.

[28] This technique is, from a computational point of view, significantly cheaper than a full 3-D approach such as the SEM [e.g., *Komatitsch and Tromp*, 2002]. The computation of synthetic seismograms at frequencies relevant to body waves (<0.1 Hz) can be computed rapidly on modest computing resources. In this study, we computed synthetic seismograms with 7 s dominant periods, which is similar to the dominant period of broadband seismograms investigated. PSVaxi and SHaxi has been used in studies of the D″ discontinuity [e.g., *Thorne et al*., 2007], global seismic scattering [*Jahnke et al*., 2008], crustal structure [*Yang et al*., 2007], and ULVZ structure modeling [*Zhang et al*., 2009].

4. Results

4.1. One-Dimensional Models

[29] Figure 6 shows the fit to δT_S and δA_S by models M1, KG10, and L2. As demonstrated previously by *Ritsema et al*. [1997], the negative *S* wave velocity gradient in the lowermost 200 km of the mantle (in M1) explains the increase of δT_S and δA_S with increasing distance. The high SV amplitudes are the result of the late onset of wave diffraction. In PREM, *S* waves begin to diffract at a distance of 100° (for a 500 km deep earthquake). Diffraction begins at a larger epicentral distance of 110° for model M1. The onset of diffraction at a relatively large distance is also evident from the relatively "sharp" SH waveforms seen at distances larger than 110° [*Ritsema et al*., 1997] (see also Figure 3). The increase of δT_S with distance is due to relatively slow *S* wave propagation through D″.

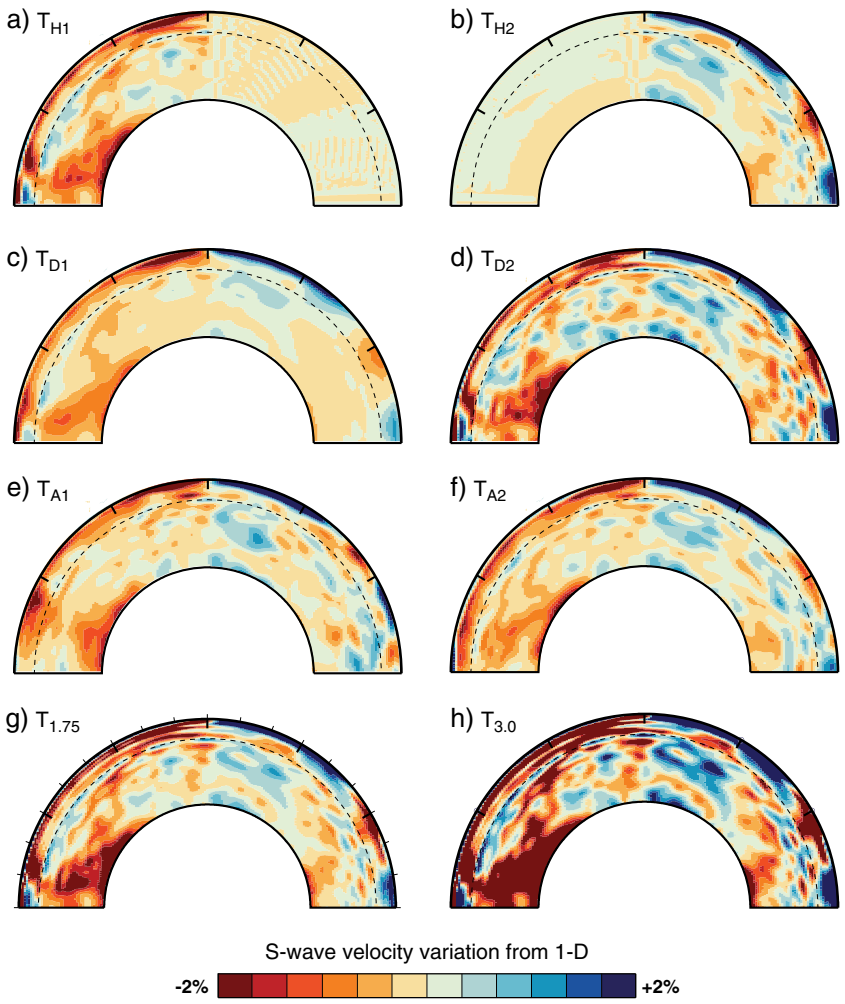

Figure 5. Cross sections (a) T_{H1}, (b) T_{H2}, (c) T_{D1}, (d) T_{D2}, (e) T_{A1}, and (f)T_{A2}. See also Table 2.

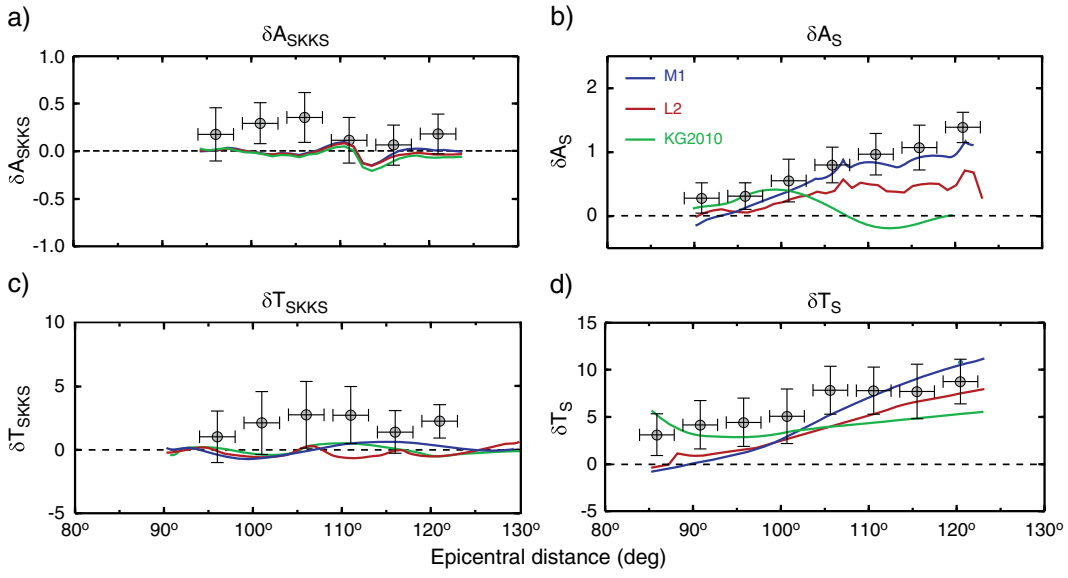

Figure 6. Observed values (Figure 4) and model predictions of δA_{SKKS}, δA_S, δT_{SKKS}, and δT_S for 1-D profiles M1 [*Ritsema et al.*, 1997], L2 [*Lay et al.*, 2006], and KG10 [*Kawai and Geller*, 2010].

[30] M1 underestimates δT_S between 85° and 105°. This indicates that the S arrival is influenced by a low S wave velocity zone above the turning depth of S waves at 85° (i.e., 2500 km). This is well above M1's low-velocity layer in the lowermost (2700–2891 km) mantle.

[31] Model L2 also predicts the increase of δT_S and δA_S with distance since it includes a low-velocity zone in the lowermost mantle with an overall vertical structure akin to M1. The negative S wave velocity gradient in L2 is weaker than in M1. Hence, the increase in δT_S and δA_S at distances larger than 100° is underestimated by L2. Since the low velocity layers in L2 are, like M1, confined to depths larger than 2700 km, L2 also fails to explain the positive δT_S values for the shortest distances. The discontinuous jumps in L2 do not affect the traveltimes and amplitudes.

[32] Model KG10 does not predict the increase with distance of either δT_S or δA_S. Although S wave velocities in KG10 are lower than that in L2 and M1, model KG10 misses a negative gradient in the lowermost mantle that is necessary to postpone the onset of S wave diffraction and hence to boost S amplitudes. The drop in δA_S between 100° and 110° is related to the strong positive S wave velocity gradient between 2600 and 2800 km depths in KG10. This is a model prediction that is inconsistent with the observations. However, in contrast to M1 and L2, model KG10 explains the positive δT_S values for the shortest distances since KG10 incorporates a strong S wave velocity reduction near the S wave turning point between 85° and 100°. This observation points to the presence of S wave velocity reductions above D″.

4.2. Three-Dimensional Models

4.2.1. The effects of the LLSVP

[33] Figures 7a–7d compares the observed amplitude and traveltime anomalies to the predictions for models T, T_{H1}, and T_{H2}. The predicted values for δA_{SKKS} are indistinguishable among the models, which demonstrates that large-scale variations of S wave velocity in the mantle have little effect on SKKS and SKS amplitudes.

[34] Model T_{H2} fails to predict the large S wave delay, predicting a slight S wave advance instead. The prediction of both T and T_{H1} match the traveltime observations, indicating that the traveltime delays are mostly due to the LLSVP in the southwest Pacific. The LLSVP in T (and T_{H1}) predicts positive values of δT_S, although the value of approximately 3 s near 85° is underestimated by both models. δT_{SKKS} and δT_S are negative for T_{H2}. Thus, the predominantly high S wave velocity structures beneath the northeastern Pacific and North America reduce the difference traveltimes by up to 2 s.

[35] The predicted values for δA_S for T_{H1} are up to 0.3 larger than for T_{H2} (Figure 7c). This indicates that the LLSVP enhances amplitudes of S diffracted waves by perturbing S wave paths through the lower mantle. Nevertheless, models T and T_{H1} underestimate δA_S considerably. It is therefore clear that the LLSVP as imaged by S40RTS does not significantly distort S wave paths in a manner that would enhance the amplitudes of diffracted waves.

4.2.2. The Effects of Damping

[36] The effects of variable tomographic damping is illustrated in Figure 7e–h. The traveltime and amplitude anomalies are slightly larger for model T_{D1} with the weakest damping and thus largest S wave velocity anomalies. The traveltime anomaly δT_{SKKS} differs most among the models. For model T_{D1}, δT_{SKKS} is up to 3 s higher than model T_{D2}. This demonstrates that the SKKS and SKS traveltime difference is influenced by the contrast in S wave velocities at the southwestern margin of the Pacific LLSVP.

[37] δT_S and δA_S are, respectively, 1–2 s and 0.2 times smaller for T_{D2}. However, the overall trends in the amplitude and traveltime predictions are similar. Therefore, an uncertainty in the strength of the S wave velocity anomalies in tomographic models does not significantly influence the interpretation of trends observed in our collection of differential traveltimes and amplitude ratios.

4.2.3. The Effects of Azimuth

[38] Similar to the effect of tomographic damping, the predicted traveltime and amplitude anomalies change little if they are computed for cross sections with slightly different azimuths. The most significant effect is seen for δT_S. The S wave velocity reduction within the LLSVP is lowest in T_{A1}. Therefore, shear waves propagating through the LLSVP as imaged by T_{A2} are not as strongly delayed as for T_{A1} and T, and thus δT_S are up to 2 s smaller. Despite the different shape of the LLSVP in cross section T_{A1}, the traveltimes and amplitude ratios are virtually identical for T_{A1} and T.

4.2.4. The Effects of Velocity Scaling

[39] The effects of scaling the low S wave velocities in T by a constant are shown in Figures 7i–7l. The stronger S wave velocity reductions produce large SKKS and S traveltime delays with respect to SKS. For each of the models tested, δT_S is larger than the observed anomalies, yet the monotonic increase in δA_S is not reproduced.

5. A Hybrid Model

[40] The model comparisons from sections 4.1 and 4.2 demonstrate that both large-scale structure (Figure 1a) and fine-scale layered structure (Figure 1b) contribute to the traveltime and amplitude anomalies. Thus, we propose a hybrid model (T_{HYB}, shown in Figure 8) for the Pacific lower mantle that incorporates the key attributes of the models. T_{HYB} explains the linear increase of δT_S and δA_S, the positive value of δT_S at relatively short distances, and the positive values of δT_{SKKS} and δA_{SKKS}. Results are summarized in Figures 8b–8e.

[41] The increase of δT_S to 10 s at 120° and of δA_S to 1.2 require the presence of a negative S wave velocity gradient in the lowermost mantle. In T_{HYB}, we included an M1 S wave velocity profile for the lowermost 200 km of the mantle, which is confined to the northeastern edge of the LLSVP (in the epicentral distance range from 40° to 60°). We applied the M1 velocity structure in this limited angular distance range such that S_{diff} raypaths interact with this negative velocity gradient, yet we do not allow the extent of the M1 structure to extend beyond the northeast boundary of the LLSVP. Because this M1 structure has a limited lateral extent, δT_S and δA_S are underestimated beyond 110°. Extending the M1 structure to an angular distance of 71° increases both δT_S and δA_S. Nevertheless, at the largest epicentral distances, these data are still underestimated. Further investigation is required to reproduce these data at the largest distances, and here we just show results where M1 extends to the LLSVP boundary.

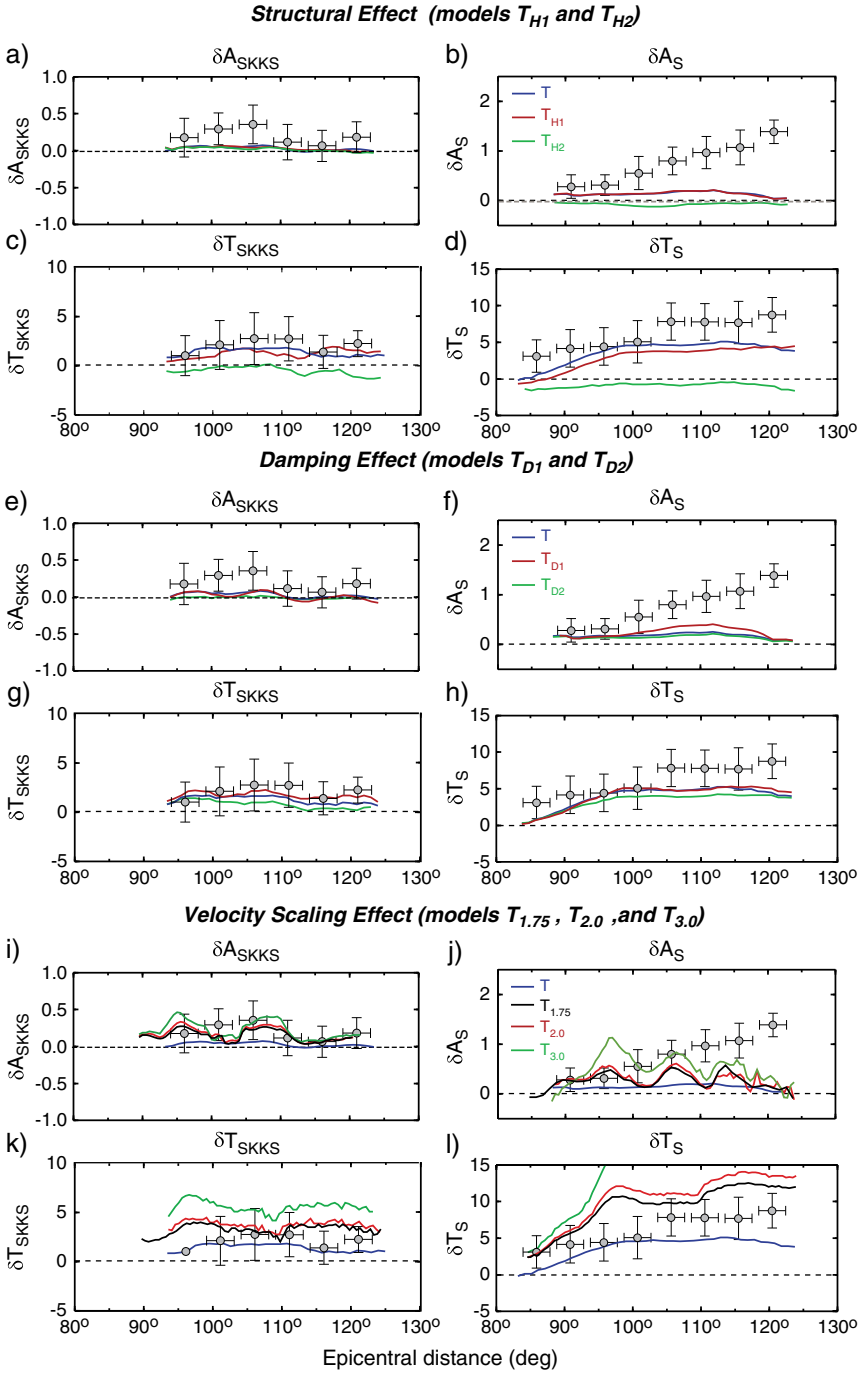

Figure 7. Measurements and model predictions of (a, e, i) δA_{SKKS}, (b, f, j) δA_S, (c, g, k) δT_{SKKS}, and (d, g, l) δT_S. Blue lines are the traveltime and amplitude predictions for T. The red lines are the prediction for T_{H1} (in a, b, c, d), T_{D1} (in e, f, g, h), and $T_{2.0}$ (in i, j, k, l). The green lines are the prediction for T_{H2} (in a, b, c, d), T_{D2} (in e, f, g, h), and $T_{3.0}$ (in i, j, k, l). The black lines are the prediction for $T_{1.75}$ (in i, j, k, l).

[42] The anomaly of δT_S of +3 s near 85° indicates a reduction of the S wave velocity well above D″. Model KG10 explains this anomaly and, as a 1-D model, places the S wave velocity reduction at the S wave turning depth of 2500 km. However, we argue that the delay is due to the LLSVP. For 85°, the S wave propagates along a roughly 1000 km long path through the center of LLSVP whereas the SKS wave (the reference phase in the δT_S measurement) skirts the southwestern margin of the LLSVP and is not delayed as strongly as S. At 85°, the δT_S measurements are slightly improved by T_{HYB} but are still underestimated. A slight decrease of the S wave velocity in the LLSVP may account for this difference as indicated by the constant velocity scaled models (Figure 7).

[43] The effect of the LLSVP on traveltimes is also clear from the δT_{SKKS} data. None of the 1-D models explain the positive values of δT_{SKKS}. Similar to our interpretation of δT_S at 85°, we interpret the positive values of δT_{SKKS} to

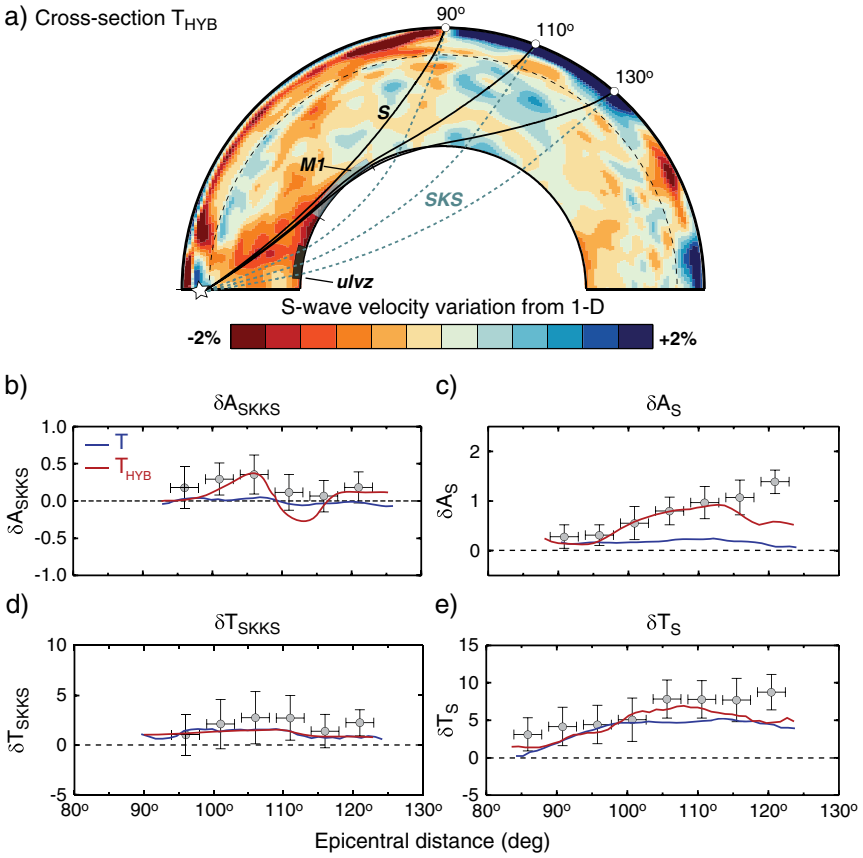

Figure 8. Measurements and model predictions of (a) δA_{SKKS}, (b) δA_{S}, (c) δT_{SKKS}, and (d) δT_{S}. The predictions are determined for cross sections (blue) T and (red) T_{HYB}.

the relatively long propagation paths of SKKS through the center of the LLSVP.

[44] None of the 1-D or 3-D models previously considered have an appreciable effect on δA_{SKKS}. To explain δA_{SKKS} anomalies, we refer to the modeling of *Zhang et al.* [2009]. They explained the increase in δA_{SKKS} by the early onset of SPdKS diffraction at the critical SKS refraction angle, consistent with the difference time between SPdKS and SKS [*Garnero and Helmberger*, 1998]. They showed that high δA_{SKKS} values can be explained by a source-side ULVZ at the base of the mantle with a thickness of 20 km and an S wave velocity reduction of 30%. In T_{HYB}, we include a ULVZ, as modeled by *Zhang et al.* [2009], embedded at the base of the LLSVP at the core-entry point of SKS. This ULVZ is 20 km thick and has 30% S wave velocity reductions. It does not strongly delay the SKS arrivals as SKS traverses the ULVZ at a steep angle.

6. Discussion and Conclusions

[45] Seismic studies of the lower mantle can be classified by tomographic and waveform modeling approaches. Low-resolution or long-wavelength (>1000 km) tomographic models are designed to explain global sets of traveltimes and only provide a large-scale perspective of velocity variations in the mantle. These models suffer in explaining amplitude variations of seismic phases due to the presence of strong velocity gradients or discontinuities. High-resolution or short-wavelength models based on regional waveform data are capable of recovering amplitude and rapid traveltime variations. While the waveform modeling approach may provide seismic velocity models at a much finer scale than tomographic models, the models are generally limited to a single sampling region and are 1-D in nature. Asymmetric velocity structure in the mantle, as present in the central Pacific region, can bias these models.

[46] In this paper, we have illustrated how a basic seismic data set can be affected by both large- and fine-scale structure. We have analyzed differential traveltimes for S-SKS (δT_{S}), SKKS-SKS (δT_{SKKS}), and the amplitude ratios S/SKS (δA_{S}) and SKKS/SKS (δA_{SKKS}) referenced to the PREM model (Figure 4). A large amount of scatter exists in these data, but they also reveal clear epicentral distance trends. The scatter is likely caused by small-scale structure in the lower mantle because earthquake mislocation and velocity heterogeneity in the uppermost mantle do not contribute strongly to the measured differential traveltimes. For example, variations in δT_{S} and δT_{SKKS} exceed 3–5 s for a given distance, which far exceeds expected signal from upper mantle sources for these differential seismic phase pairs. As simulated traveltimes and amplitudes for the range of tomographic models and 1-D velocity profiles tested in this study (Figure 7) reproduce only a fraction of the observed variability, it is also unlikely that the observed scatter is due to large-scale structural features.

[47] The epicentral distance variation of the differential traveltimes and amplitude ratios is due to both the large-scale structure of the lower mantle and fine-scale layering

in D″. Nonzero values of δT_{SKKS} and δT_S (at 85°) cannot be explained by 1-D seismic profiles. Using S40RTS as a guide (Figure 2), we associate the delays of S and SKKS with respect to SKS to the presence of the Pacific LLSVP. S and SKKS propagate through the center of the Pacific LLSVP while SKS skirts its southwestern margin. As a consequence, the LLSVP slows down S and SKKS but it has no, or a much smaller, effect on SKS.

[48] The LLSVP does not explain the anomalous δA_S and δA_{SKKS} amplitude ratios. A minor increase in δA_S can be accomplished by strengthening the shear-velocity reductions within the LLSVP. Models $T_{2.0}$ and $T_{3.0}$, with 2× and 3× stronger LLSVP velocity reductions than S40RTS, respectively, match δA_S up to 105° (Figure 7j). However, these models do not reproduce the monotonic increase of δA_S, and they overpredict δT_S for all distances. It is much more likely that an *S* wave gradient in D″ is responsible for the high *S* wave amplitudes. Model M1, which includes a negative *S* wave velocity gradient in D″, explains both the high *S* wave amplitudes and the delayed δT_S traveltimes. *S* waves propagating through an M1 structure begin to diffract around the core at an epicentral distance of approximately 110° (instead of 100° for PREM). As a consequence, the amplitudes of SV do not decay as quickly as for PREM (hence δA_S is anomalously high).

[49] We interpret the anomalous values of δA_{SKKS} to a 20 km thick ULVZ at the base of the mantle, which separates SPdKS from SKS [e.g., *Garnero et al*., 1998; *Thorne and Garnero*, 2004] at an earlier distance than that in PREM and causes the SKS amplitude to drop [*Zhang et al*., 2009]. This region is also noted for strong scattering of short-period arrivals (e.g., PKP, PKKP) [*Cormier*, 2000; *Hedlin and Shearer*, 2000], which may also be linked to ULVZs. It must be emphasized, however, that a significant portion of the lower mantle is as yet unexplored for potential scatterers and their relation to ULVZs.

[50] Our work implies that the interpretation of 1-D and 3-D images of the mantle is difficult. Many interesting observations have been made regarding the nature of and/or consequences of LLSVPs. For example, *Garnero and McNamara* [2008] suggested that ULVZs may be concentrated at the edges of LLSVPs. This suggests a relationship between LLSVPs and dynamic processes such as the formation of plumes. Yet, it is questionable whether boundaries between high and low *S* wave velocities in tomographic images such as S40RTS represent sharp edges of LLSVPs. In T_{HYB}, we place the M1 structure in a limited angular range based on the lateral extent of the LLSVP in S40RTS. However, T_{HYB} does not match δT_S and δA_S for distances larger than 110°, possibly because the edge of the LLSVP is located further to the northeast than imaged in S40RTS.

[51] Similarly, seismic modeling using 1-D profiles can be biased by the presence of 3-D seismic velocity heterogeneity. Model KG10 [*Kawai and Geller*, 2010] has a velocity reduction of approximately 2.8% at the depth of 2550 km. This feature explains the delay of ScS with respect to S as analyzed by *Kawai and Geller* [2010] and the delay of δT_S at 85° as discussed in this paper. *Kawai and Geller* [2010] interpreted this strong low velocity zone as due to phase transitions in the mineral structure of pervoskite. Alternatively, the ScS-S and S-SKS delays may be related to the LLSVP that has a stronger effect on S than ScS and SKS.

[52] Large-scale mantle structure, as resolved through tomographic efforts, causes regional-scale traveltime variability; thus, studies analyzing fine-scale structure within D″ cannot exclude these large-scale mantle features. Conversely, the fine-scale structures imaged through forward modeling approaches are capable of explaining relative amplitude measurements that are not currently captured in the tomographic models. Full 3-D waveform tomographic approaches are being developed [*Hara*, 2004; *Tape et al*., 2009; *Fichtner et al*., 2009]. However, on the global scale, these are still limited to relatively low-frequencies given the computational demands. To capture both the large-scale and small-scale seismic structure of the mantle, as discussed here for the Pacific, it is likely that the modeling of high-frequency body wave signals must involve iterative forward modeling. Overall, we recommend a combined approach of analyzing both traveltime and amplitude ratios to capture the "real" velocity of structure of the CMB region. Although extensive forward modeling is required to arrive at hybrid models as presented in this paper, we emphasize that the *S* wave velocity structure of the Pacific lower mantle cannot be fully described by either global tomographic or regional modeling approaches in exclusion.

[53] **Acknowledgments.** The authors gratefully acknowledge the University of Utah Center for High Performance Computing (CHPC) for computer resources and support. They thank V. Cormier and C. Houser for their constructive review and suggestions. MT, JR, and YZ were partially supported by the National Science Foundation (grant no. EAR-1014749). Seismic data were provided by the IRIS Data Management Center. Figures were drawn using the Generic Mapping Tools [*Wessel and Smith*, 1998).

References

Bull, A. L., A. K. McNamara, and J. Ritsema (2009), Synthetic tomography of plume clusters and thermochemical piles, *Earth Planet. Sci. Lett.*, *278*, 152–162.

Cormier, V. (2000), D″ as a transition in the heterogeneity spectrum of the lowermost mantle, *J. Geophys. Res.*, *105*, 16,193–16,205.

Davies, D. R., S. Goes, J. H. Davies, B. S. A. Schuberth, H.-P. Bunge, and J. Ritsema (2012), Reconciling dynamic and seismic models of earth's lower mantle: the dominant role of thermal heterogeneity, *Earth Planet. Sci. Lett.*, 253–269, doi:10.1016/j.epsl.2012.08.016.

Dziewonski, A. M., and D. L. Anderson (1981), Preliminary Reference Earth Model, *Phys. Earth Planet. Inter.*, *25*, 297–356.

Dziewonski, A. M., V. Lekic, and B. A. Romanowicz (2010), Mantle Anchor Structure: An argument for bottom up tectonics, *Earth Planet. Sci. Lett.*, *299*(1–2), 69–79.

Fichtner, T., B. Kennett, H. Igel, and H.-P. Bunge (2009), Full seismic waveform tomography for upper-mantle structure in the Australasian region using adjoint methods, *Geophys. J. Int.*, *179*, 1365–246X, doi:10.1111/j.1365-246X.2009.04368.x.

Ford, S., E. Garnero, and A. McNamara (2006), A strong lateral shear velocity gradient and anisotropy heterogeneity in the lowermost mantle beneath the southern Pacific, *J. Geophys. Res.*, *111*(B3), doi:10.1029/2004JB003574.

Furumura, T., B. L. N. Kennett, and M. Furumura (1998), Synthetic seismograms for a laterally heterogeneous whole earth model by the pseudospectral method, *Geophys. J. Int.*, *135*, 845–860.

Garnero, E., and D. Helmberger (1998), Further structural constraints and uncertainties of a thin laterally varying ultralow-velocity layer at the base of the mantle, *J. Geophys. Res.*, *103*(B6), 12,495–12,509.

Garnero, E. J., J. Revenaugh, Q. Williams, T. Lay, and L. H. Kellogg (1998), Ultralow velocity zone at the core-mantle boundary, in *The Core-Mantle Boundary Region*, edited by M. Gurnis, M. Wysession, E. Knittle, and B. A. Buffett, pp. 319–334, American Geophysical Union, Washington, D. C.

Garnero, E. J., and A. K. McNamara (2008), Structure and dynamics of Earth's lower mantle, *Science*, *320*, 626–628.

Grand, S. P. (1994), Mantle shear structure beneath the america and surrounding oceans, *J. Geophys. Res.*, *99*, 11,591–11,621.

Hara, T. (2004), Waveform inversion for 3-D earth structure using the Direct Solution Method implemented on vector-parallel supercomputer,

Phys. Earth Planet. Inter., *146*(1–2), 65–74, doi:10.1016/j.pepi.2003.06.010.

He, Y., and L. Wen (2009), Structural features and shear-velocity structure of the "Pacific Anomaly", *J. Geophys. Res.*, *114*, doi:10.1029/2008JB005814.

Hedlin, M., and P. Shearer (2000), An analysis of large-scale variations in small-scale mantle heterogeneity using Global Seismographic Network recordings of precursors to PKP, *J. Geohys. Res.*, *105*, 13,655–13,673.

Hernlund, J. W., and P. J. Tackley (2007), Some dynamical consequences of partial melting in Earth's deep mantle, *Phys. Earth Planet. Inter.*, *162*(1–2), 149–163.

Hernlund, J. W., C. Thomas, and P. J. Tackley (2005), A doubling of the post-perovskite phase boundary and structure of the Earth's lowermost mantle, *Nature*, *434*, 882–886, doi:10.1038/nature03472.

Hutko, A. R., T. Lay, and J. Revenaugh (2009), Localized double-array stacking analysis of PcP: D″ and ULVZ structure beneath the Cocos plate, Mexico, central Pacific, and north Pacific, *Phys. Earth Planet. Inter.*, *173*(1–2), 60–74.

Igel, H., and M. Weber (1996), P-SV wave propagation in the Earth's mantle using finite differences: Application to heterogeneous lowermost mantle structure, *Geophys. Res. Lett.*, *23*, 415–418.

Jahnke, G., M. S. Thorne, A. Cochard, and H. Igel (2008), Global SH-wave propagation using a parallel axisymmetric spherical finite-difference scheme: application to whole mantle scattering, *Geophys. J. Int.*, *173*(3), 815–826.

Kawai, K., and R. J. Geller (2010), Waveform inversion for localized seismic structure and an application to D″ structure beneath the Pacific, *J. Geophys. Res.*, *115*, doi:10.1029/2009JB006503.

Komatitsch, D., and J. Tromp (2002), Spectral-element simulations of global seismic wave propagation-I. Validation, *Geophys. J. Int.*, *149*(2), 390–412, doi:10.1046/j.1365-246X.2002.01653.x.

Lay, T., and E. J. Garnero (2011), Deep mantle seismic modeling and imaging, *Annu. Rev. Earth Planet. Sci.*, *39*, 91–123, doi:10.1146/annurev-earth-040610-133354.

Lay, T., J. Hernlund, E. J. Garnero, and M. S. Thorne (2006), A post-perovskite lens and D '' heat flux beneath the central Pacific, *Science*, *314*(5803), 1272–1276.

Ni, S., and D. Helmberger (2003), Seismological constraints on the South African superplume; could be the oldest distinct structure on Earth, *Earth Planet. Sci. Lett.*, *206*(1–2), 119–131.

Ni, S., X. Ding, and D. V. Helmberger (2000), Constructing synthetics from deep earth tomographic models, *Geophys. J. Int.*, *140*, 71–82.

Ni, S., D. Helmberger, and J. Tromp (2005), Three-dimensional structure of the African superplume from waveform modelling, *Geophys. J. Int.*, *161*(2), 283–294.

Pulliam, J., and M. K. Sen (1998), Anisotropy in the core-mantle transition zone may indicate chemical heterogeneity, *Geophys. J. Int.*, *135*, 113–128.

Ritsema, J., E. Garnero, and T. Lay (1997), A strongly negative shear velocity gradient and lateral variability in the lowermost mantle beneath the Pacific, *J. Geophys. Res.*, *102*, 20,395–20,411.

Ritsema, J., A. K. McNamara, and A. L. Bull (2007), Tomographic filtering of geodynamic models: Implications for model interpretation and large-scale mantle structure, *J. Geophys. Res.*, *112*, B0130, doi:10.1029/2006JB004566.

Ritsema, J., A. Deuss, H. J. van Heijst, and J. H. Woodhouse (2011), S40rts: a degree-40 shear-velocity model for the mantle from new rayleigh wave dispersion, teleseismic traveltime and normal-mode splitting function measurements, *Geophys. J. Int.*, doi:10.1111/j.1365-246X.2010.04884.x.

Rondenay, S., V. F. Cormier, and E. M. V. Ark (2010), SKS and SPdKS sensitivity to two-dimensional ultralow-velocity zones, *J. Geophys. Res.*, *115*, doi:10.1029/2009JB006733.

Rost, S., and C. Thomas (2009), Improving seismic resolution through seismic arrays, *Surv. Geophys.*, *30*(4–5), 271–299, doi:10.1007/s10712-009-9070-6.

Russell, S., C. Reasoner, T. Lay, and J. Revenaugh (2001), Coexisting shear- and compressional-wave seismic velocity discontinuities beneath the central Pacific, *Geophys. Res. Lett.*, *28*(11), 2281–2284.

Schuberth, B. S. A., H.-P. Bunge, and J. Ritsema (2009), Tomographic filtering of mantle circulation models: can seismic heterogeneity be explained by temperature variations alone?, *Geochem. Geophys. Geosys.*, *5*, doi:10.1029/2004GC000807.

Schutt, D., and E. Humphreys (2001), Evidence for a deep asthenosphere beneath North America from western united states SKS splits, *Geology*, *29*(4), 291–294.

Simmons, N. A., A. M. Forte, and S. P. Grand (2009), Joint seismic, geodynamic and mineral physical constraints on three-dimensional mantle heterogeneity: Implications for the relative importance of thermal versus compositional heterogeneity, *Geophys. J. Int.*, *177*, 1284–1304.

Sun, D., D. Helmberger, and M. Gurnis (2010), A narrow, mid-mantle plume below southern Africa, *Geophys. Res. Lett.*, *37*, L09302, doi:10.1029/2009GL042339.

Takeuchi, N., Y. Morita, N. D. Xuyen, and N. Q. Zung (2008), Extent of the low-velocity region in the lowermost mantle beneath the western pacific detected by the vietnamese broadband seismograph array, *Geophys. Res. Lett.*, *35*, doi:10.1029/2008GL033197.

Tanaka, S. (2002), Verv low shear wave velocitv at the base of the mantle under the South Pacific Superswell, *Earth Planet. Sci. Lett.*, *203*(3–4), 879–893.

Tape, C., Q. Liu, A. Maggi, and J. Tromp (2009), Adjoint Tomography of the Southern California Crust, *Science*, *325*(5943), 988–992, doi:10.1126/science.1175298.

Thorne, M., T. Lay, E. Garnero, G. Jahnke, and H. Igel (2007), Seismic imaging of the laterally varying D″ region beneath the Cocos Plate, *Geophys. J. Int.*, *170*, 635–648, doi:10.1111/j.1365-246X.2006.03279.x.

Thorne, M. S., and E. J. Garnero (2004), Inferences on ultralow-velocity zone structure from a global analysis of spdks waves, *J. Geophys. Res.*, *109*, doi:10.1029/2004JB003010.

To, A., B. Romanowicz, Y. Capdeville, and N. Takeuchi (2005), 3D effects of sharp boundaries at the borders of the African and Pacific Superplumes: Observation and modeling, *Earth Planet. Sci. Lett.*, *233*(1–2), 137–153.

Trampert, J., F. Deschamps, J. Resovsky, and D. Yuen (2004), Probabilistic tomography maps chemical heterogeneities throughout the lower mantle, *Science*, *306*, 853–856.

Tsuchiya, T., and J. Tsuchiya (2006), Effect of impurity on the elasticity of perovskite and postperovskite: Velocity contrast across the postperovskite transition in (Mg,Fe,Al)(Si,Al)O3, *Geophys. Res. Lett.*, *33*, doi:10.1029/2006GL025706.

Tsuchiya, T., J. Tsuchiya, K. Umemoto, and R. M. Wentzcovitch (2004), Elasticity of post-perovskite MgSiO3, *Geophys. Res. Lett.*, *31*, doi:10.1029/2004GL020278.

Wessel, P., and W. H. F. Smith (1998), New, Improved Version of Generic Mapping Tools Released, *Eos, Trans. Amer. Geophys. Union*, *79*, 579.

Williams, Q., and E. Garnero (1996), Seismic evidence for partial melt at the base of Earth's mantle, *Science*, *273*(5281), 1528–1530.

Yang, X., T. Lay, X.-B. Xie, and M. S. Thorne (2007), Geometric spreading of pn and sn in a spherical earth model, *Bull. Seismol. Soc. Am.*, *97*(6), 2053–2065, doi:10.1785/0120070031.

Zhang, Y., J. Ritsema, and M. Thorne (2009), Modeling the ratios of SKKS and SKS amplitudes with ultra-low velocity zones at the core-mantle boundary, *Geophys. Res. Lett.*, *36*, doi:10.1029/2009GL040030.